



Supplement of

Dependency of the impacts of geoengineering on the stratospheric sulfur injection strategy – Part 2: How changes in the hydrological cycle depend on the injection rate and model used

Anton Laakso et al.

Correspondence to: Anton Laakso (anton.laakso@fmi.fi)

The copyright of individual parts of the supplement might differ from the article licence.

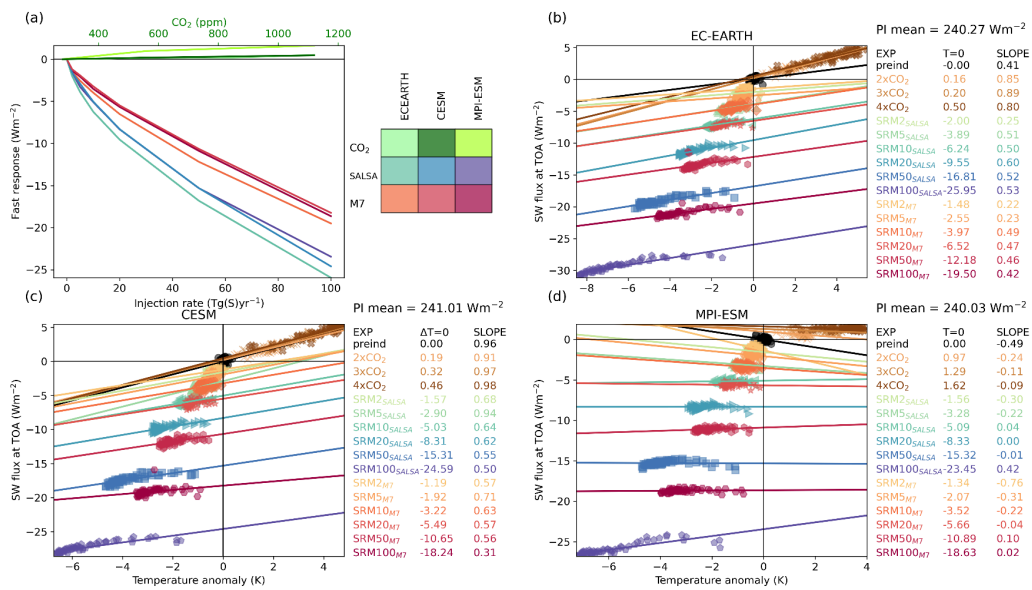


Figure S1. a) Fast response of shortwave radiative flux change at the top of the atmosphere (i.e radiative forcing) in simulations of different CO₂ concentration and stratospheric sulfur injections. Gregory plots of the shortwave radiative flux change in studied scenarios in b) EC-EARTH, c) CESM and d) MPI-ESM.

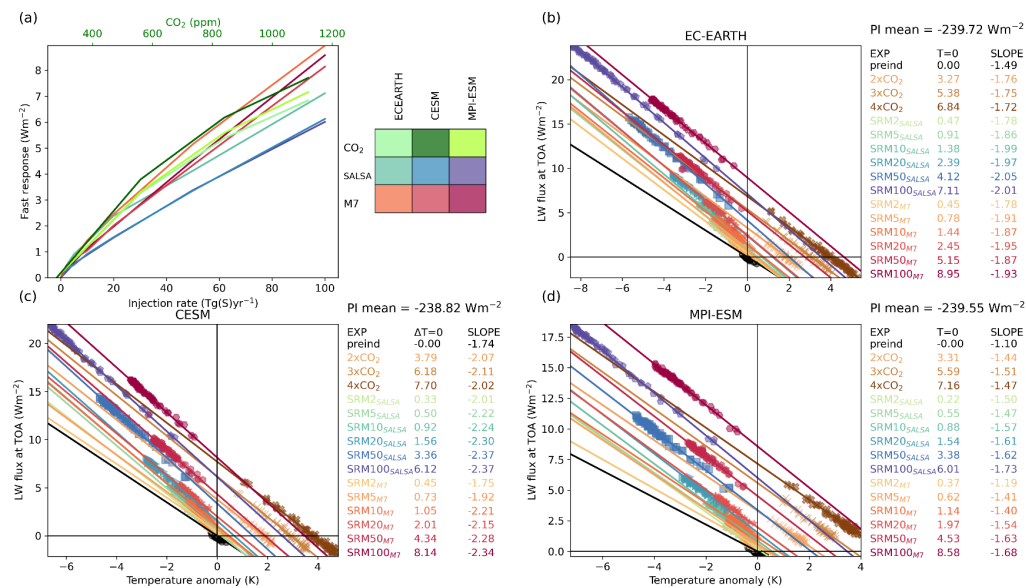


Figure S2. a) Fast response of longwave radiative flux change at top of the atmosphere (i.e radiative forcing) in simulations of different CO₂ concentration and stratospheric sulfur injections. Gregory plots of the longwave radiative flux change in studied scenarios in b) EC-EARTH, c) CESM and d) MPI-ESM.

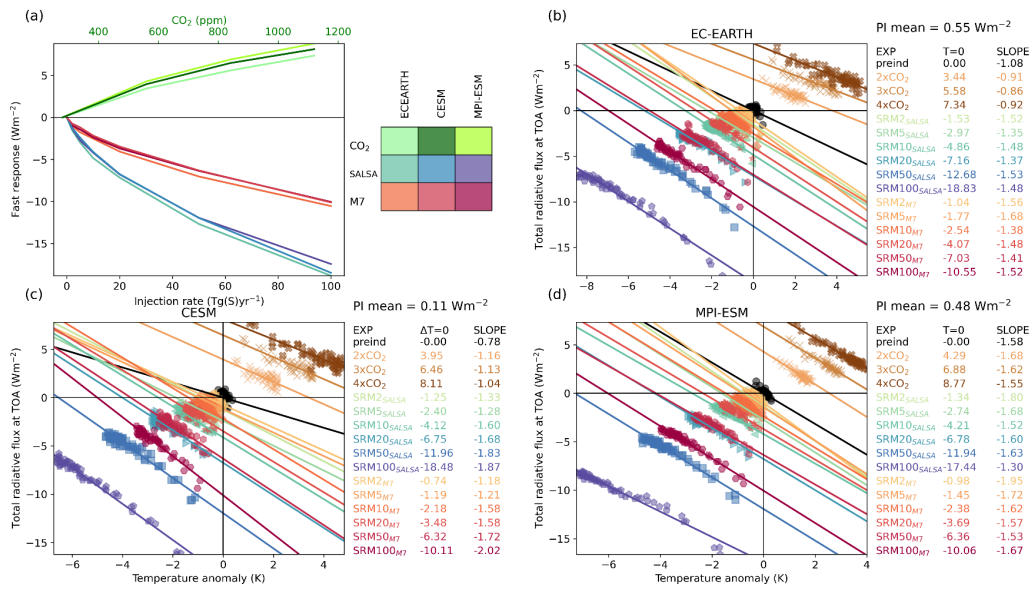


Figure S3. a) Fast response of total (shortwave + longwave) radiative flux change (i.e radiative forcing) in simulations of different CO₂ concentration and stratospheric sulfur injections. Gregory plots of the total radiative flux change in studied scenarios in b) EC-EARTH, c) CESM and d) MPI-ESM.

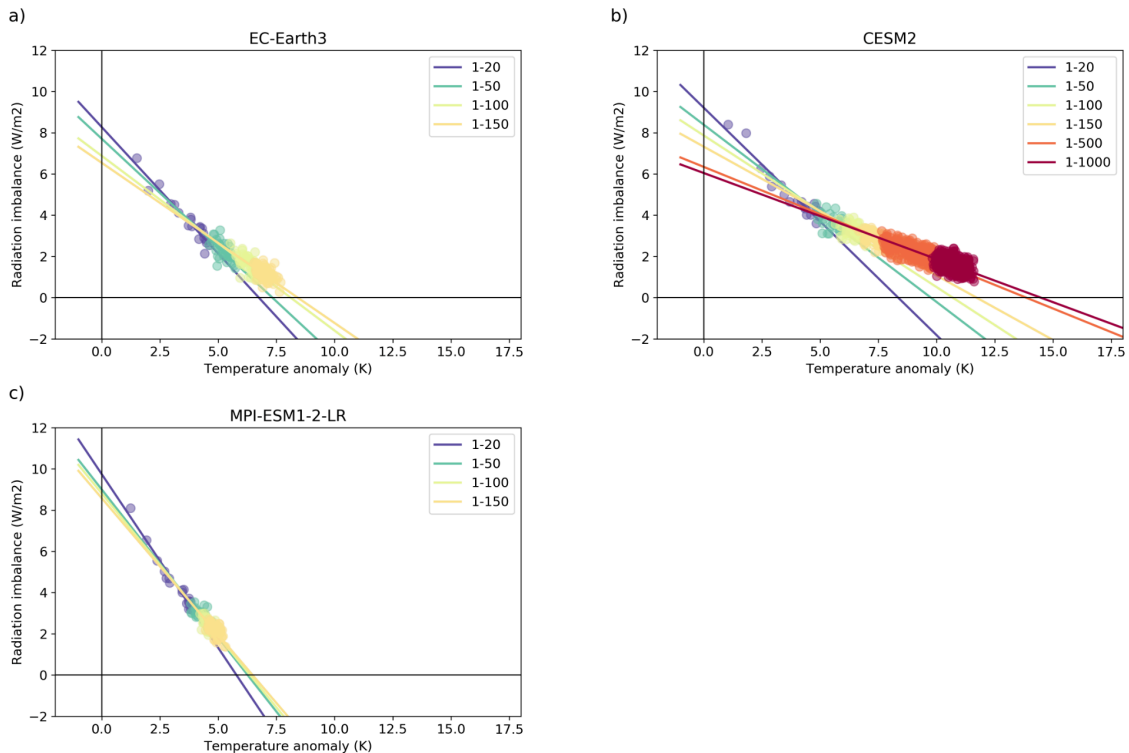


Figure S4. Effective climate sensitivity based on the years used for making a fit in a) EC-EARTH, b) CESM and c) MPI-ESM based on 4xCO₂ scenario for CMIP6.

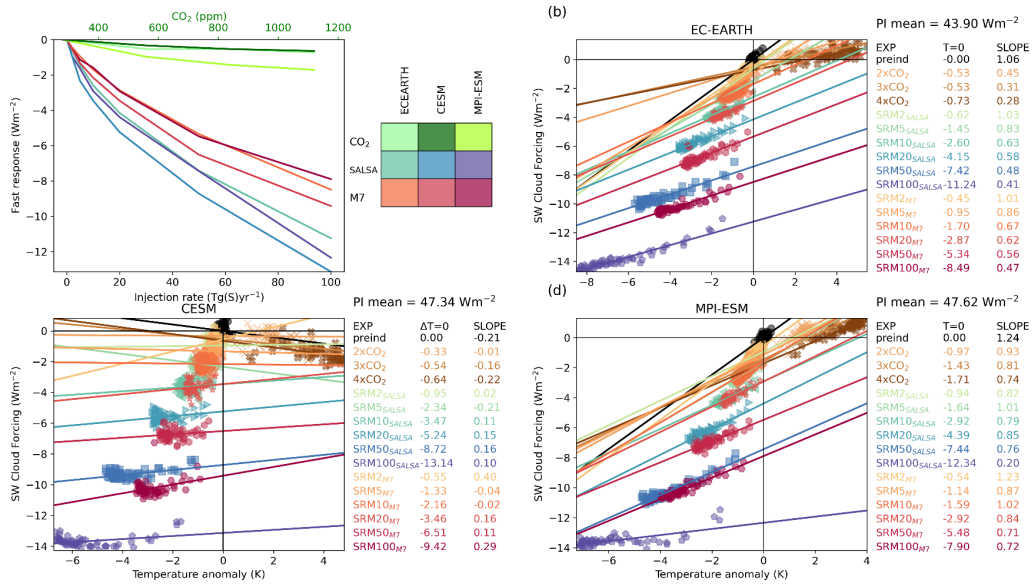


Figure S5. a) Fast shortwave cloud forcing in simulations of different CO₂ concentration and stratospheric sulfur injections. Regression plots of the SW cloud forcing change in studied scenarios in b) EC-EARTH, c) CESM and d) MPI-ESM. Impact of clouds on SW radiation is calculated as the difference between cloud free SW radiation flux and SW radiation flux (including clouds) at the top of the atmosphere. Note that interaction between clouds and SW radiation is significantly reduced due to stratospheric aerosols.

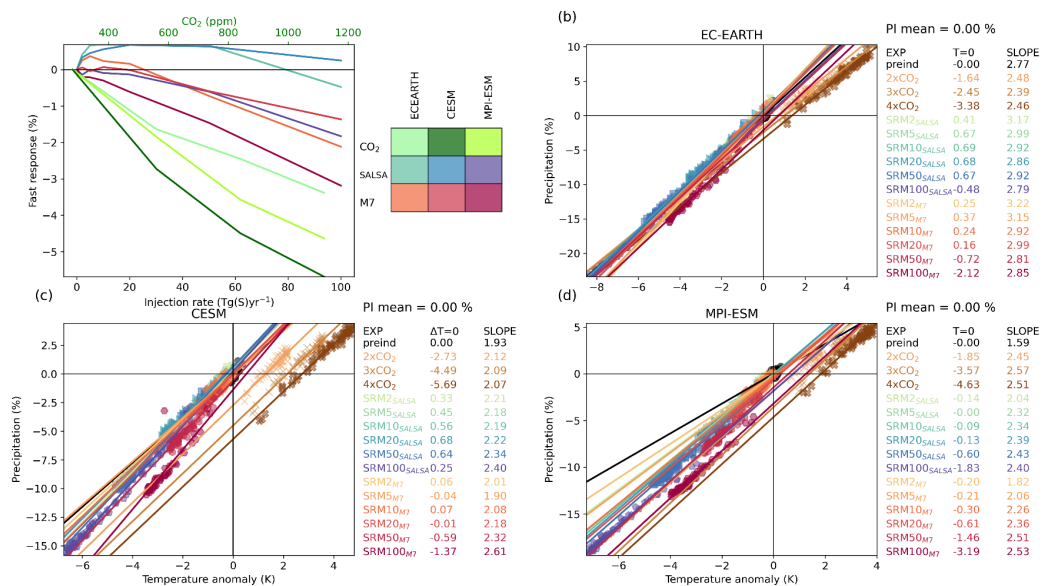


Figure S6. a) Fast precipitation response in simulations of different CO₂ concentration and stratospheric sulfur injections. Regression plots of the precipitation change in studied scenarios in b) EC-EARTH, c) CESM and d) MPI-ESM.

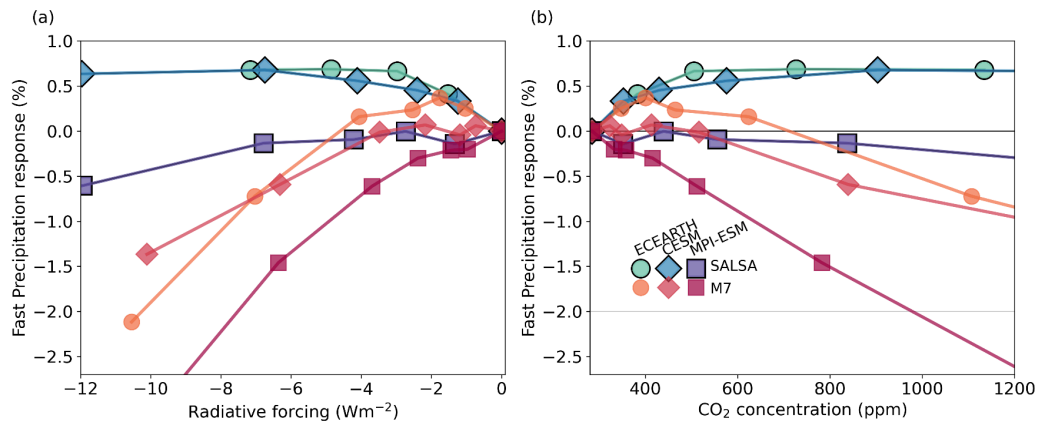


Figure S7. a) Fast precipitation response as a function radiative forcing of SAI with different injection rates and b) fast precipitation response of SAI in climate equilibrium scenarios.

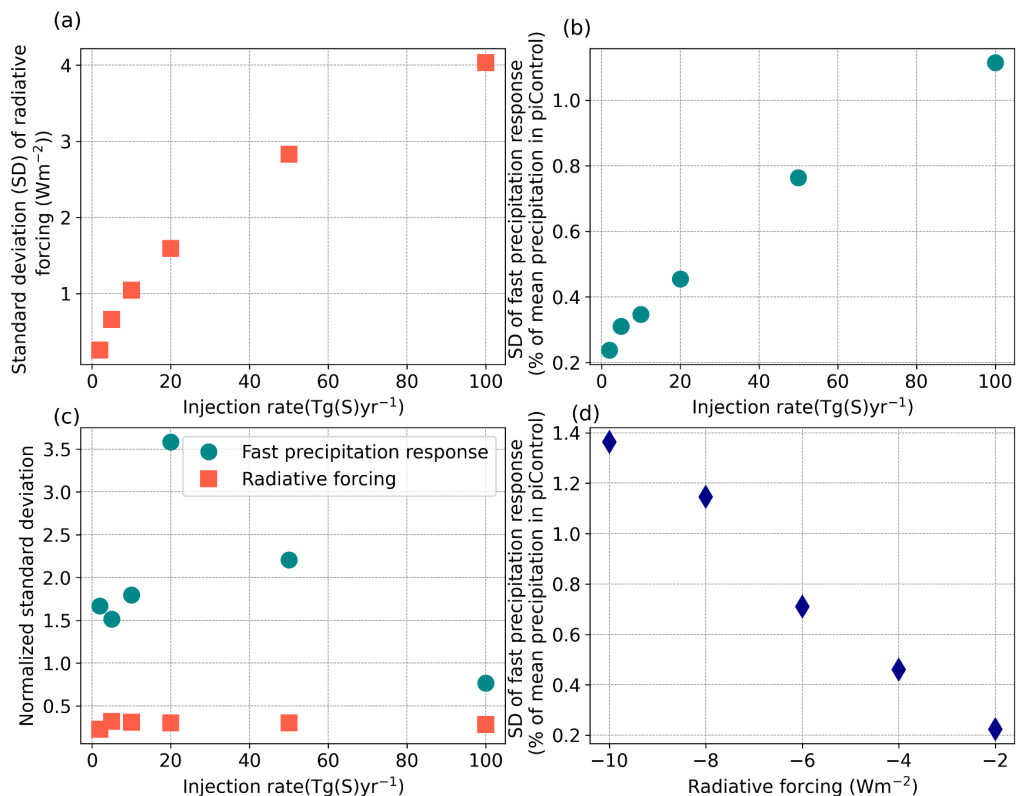


Figure S8. Standard deviation (SD) of simulated a) radiative forcing at TOA and b) fast precipitation response as a function of injection rate, c) coefficient of variation of radiative forcings and d) fast precipitation responses and SD of fast precipitation responses as a

function of injection rate. Since specific radiative forcings marked in d) are not simulated, the fast precipitation responses are estimated based on the two closest simulated radiative forcings.

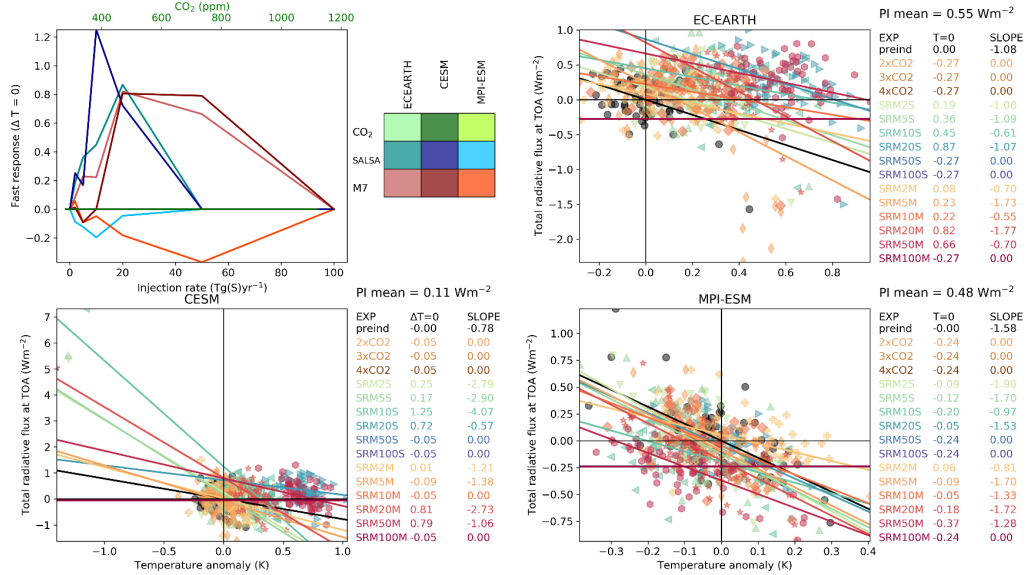


Figure S9. Gregory plots of the total radiative flux change in climate equilibrium scenarios (see Table 1.) where radiative forcing from increased CO₂ concentration and SAI are hypothetically compensating each other.

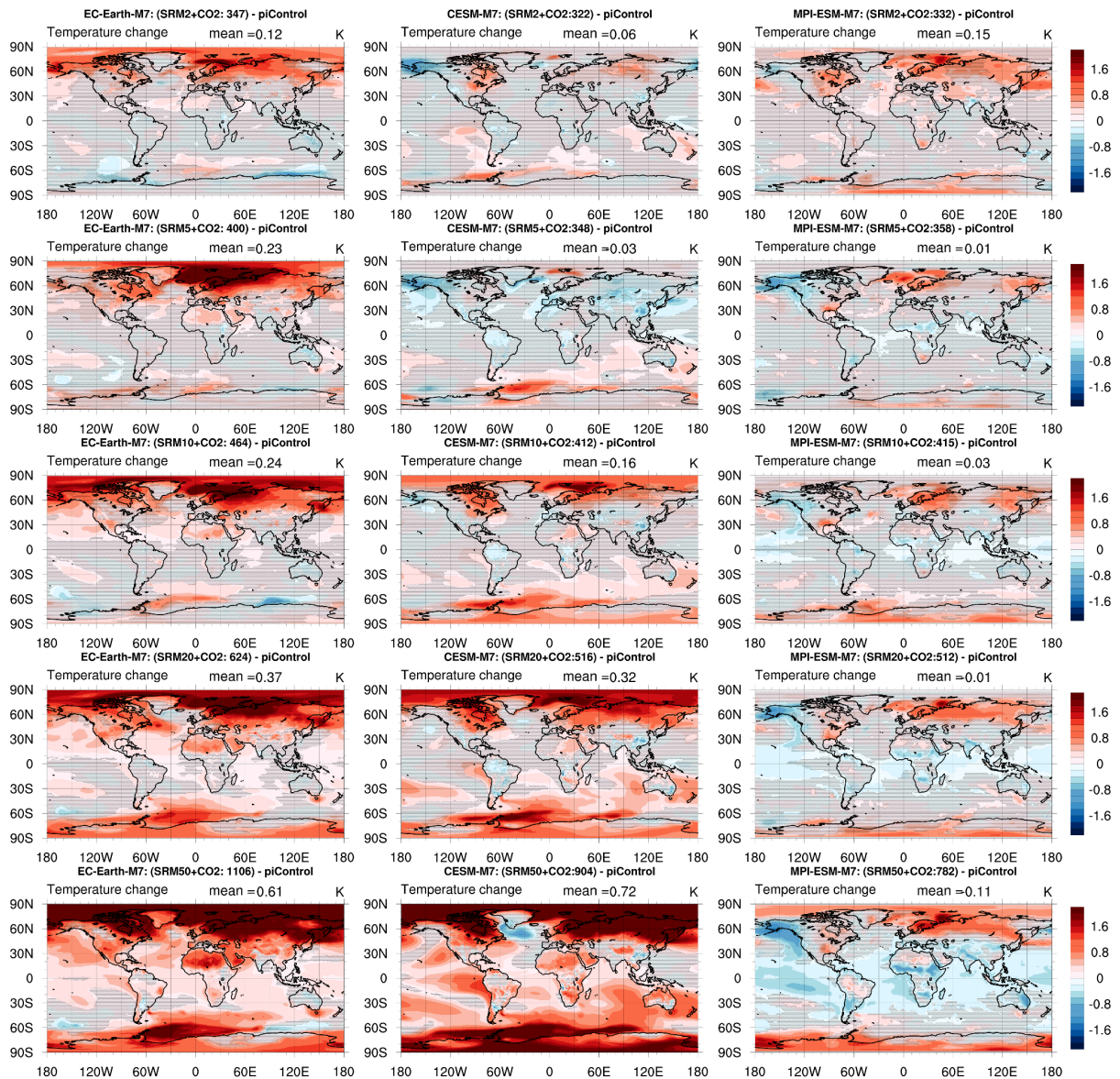


Figure S10. Differences in regional temperature patterns between the climate equilibrium scenarios where M7 aerosols are used and piControl scenario. EC-Earth results are in the left column, CESM results are in the middle and MPI-ESM results are in the right column. Hatching indicates regions where the temperature change is not statistically significant based on the Wilcoxon signed-rank test (p -value < 0.05).

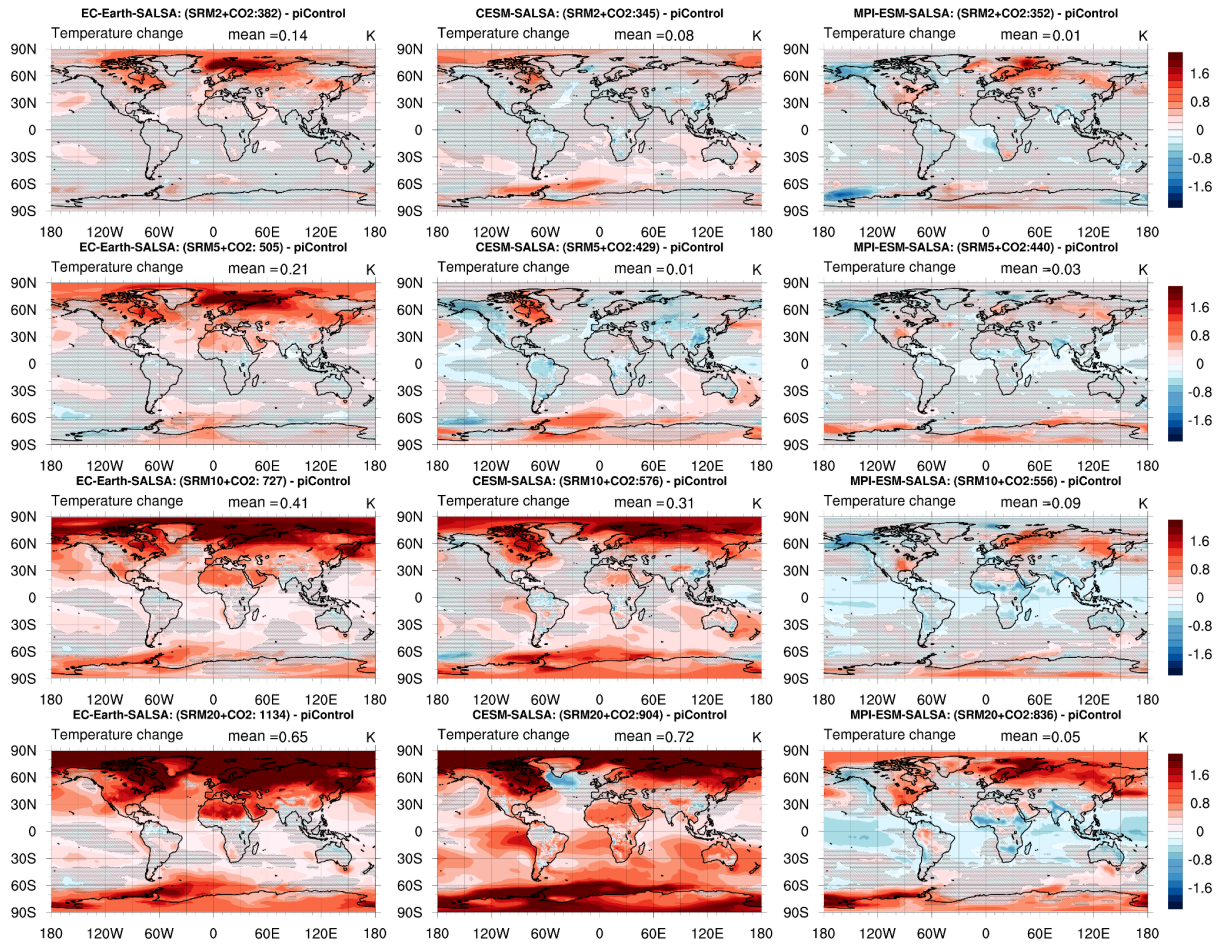


Figure S11. Differences in regional temperature patterns between the climate equilibrium scenarios where SALSA aerosols are used and piControl scenario. EC-Earth results are in the left column, CESM results are in the middle and MPI-ESM results are in the right column. Hatching indicates regions where the temperature is not statistically significant based on the Wilcoxon signed-rank test (p -value < 0.05).

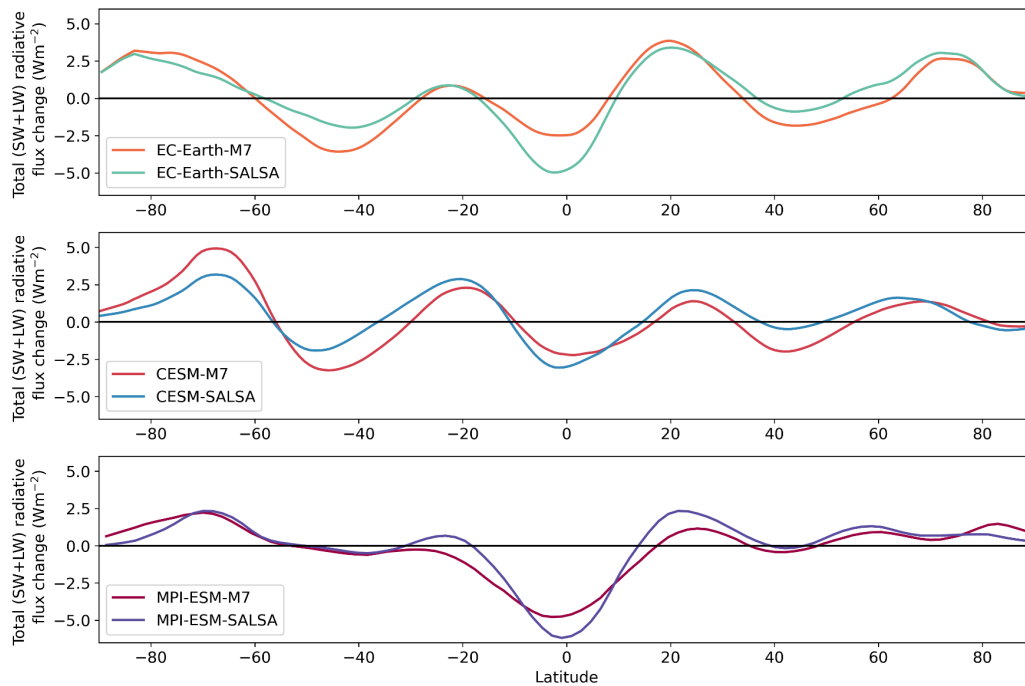


Figure S12. Total zonal mean (SW+LW) radiative flux change in equilibrium simulation with 20 Tg(S) injection and corresponding CO₂ concentration to have presumptive climate equilibrium. Flux changes are calculated based on the first 5 years and compared to piControl. To reduce fluctuation in the line, shown values are mean values from 14° wide area.

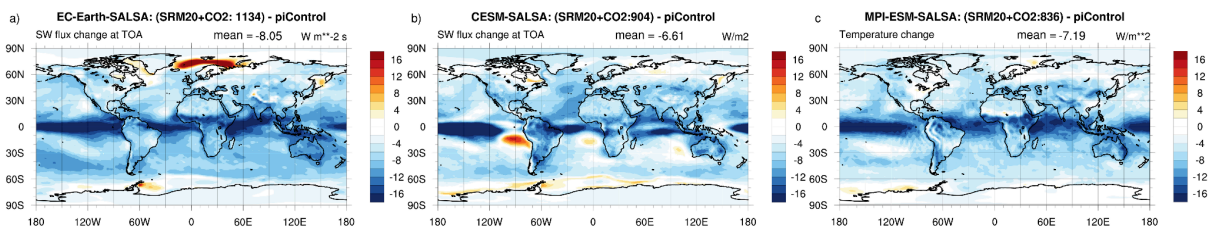


Figure S13. Change in SW radiation fluxes at the top of the atmosphere in equilibrium simulation with 20 Tg(S)/yr injection and corresponding CO₂ concentration to have presumptive climate equilibrium. Figure shows mean values of analyzed period (30 last years of the simulations).

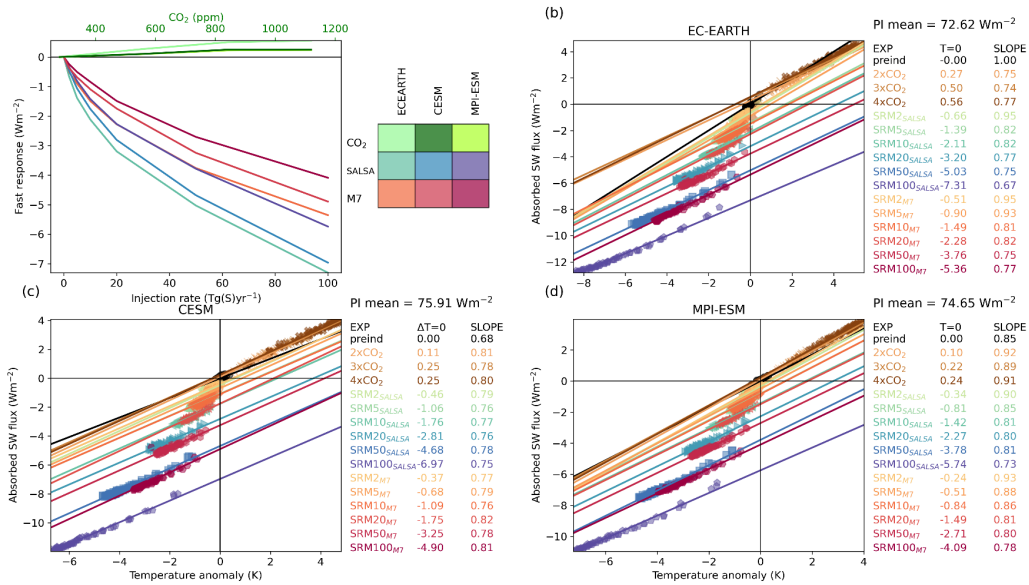


Figure S14. a) Absorption part of SW radiative forcing. Regression plots of the atmospheric absorption for SW radiation in studied scenarios in b) EC-EARTH, c) CESM and d) MPI-ESM.

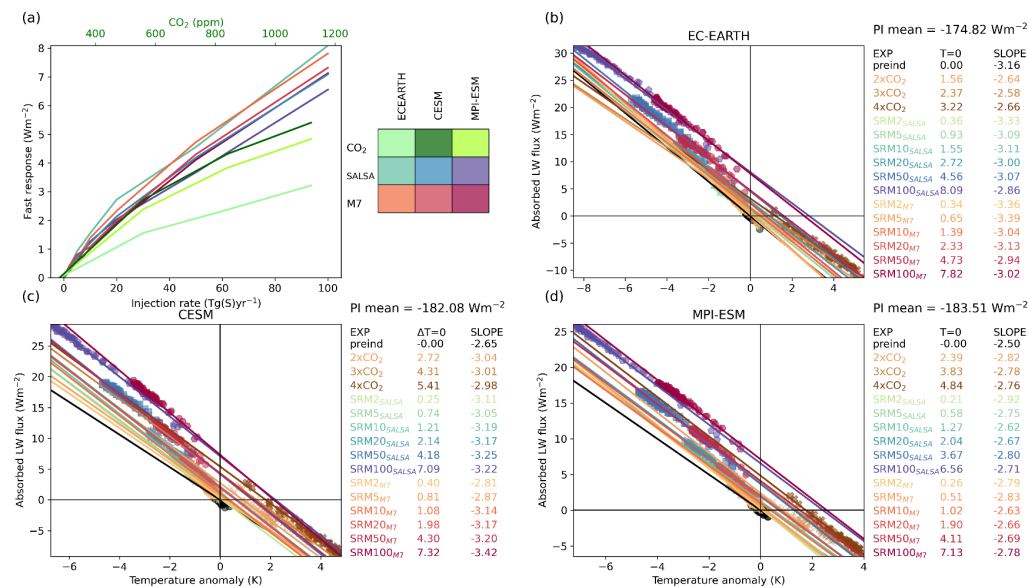


Figure S15. a) Absorption part of LW radiative forcing. Regression plots of the atmospheric absorption for LW radiation in studied scenarios in b) EC-EARTH, c) CESM and d) MPI-ESM.

| | SW (Wm^{-2}) | | | LW (Wm^{-2}) | | | Total (SW+LW) (Wm^{-2}) | | |
|-------------------------|------------------|-------|---------|------------------|------|---------|-----------------------------|-------|---------|
| | EC-Earth | CESM | MPI-ESM | EC-Earth | CESM | MPI-ESM | EC-Earth | CESM | MPI-ESM |
| SRM2 _{SALSA} | -0.66 | -0.46 | -0.34 | 0.36 | 0.25 | 0.21 | -0.3 | -0.21 | -0.13 |
| SRM5 _{SALSA} | -1.39 | -1.06 | -0.81 | 0.93 | 0.74 | 0.58 | -0.46 | -0.32 | -0.23 |
| SRM10 _{SALSA} | -2.11 | -1.76 | -1.42 | 1.55 | 1.21 | 1.27 | -0.56 | -0.55 | -0.15 |
| SRM20 _{SALSA} | -3.2 | -2.81 | -2.27 | 2.72 | 2.14 | 2.04 | -0.48 | -0.67 | -0.23 |
| SRM50 _{SALSA} | -5.03 | -4.68 | -3.78 | 4.56 | 4.18 | 3.67 | -0.47 | -0.5 | -0.11 |
| SRM100 _{SALSA} | -7.31 | -6.97 | -5.74 | 8.09 | 7.09 | 6.56 | 0.78 | 0.12 | 0.82 |
| SRM2 _{M7} | -0.51 | -0.37 | -0.24 | 0.34 | 0.4 | 0.26 | -0.17 | 0.03 | 0.02 |
| SRM5 _{M7} | -0.9 | -0.68 | -0.51 | 0.65 | 0.81 | 0.51 | -0.25 | 0.13 | 0 |
| SRM10 _{M7} | -1.49 | -1.09 | -0.84 | 1.39 | 1.08 | 1.02 | -0.1 | -0.01 | 0.18 |
| SRM20 _{M7} | -2.28 | -1.75 | -1.49 | 2.33 | 1.98 | 1.9 | 0.05 | 0.23 | 0.41 |
| SRM50 _{M7} | -3.76 | -3.25 | -2.71 | 4.73 | 4.03 | 4.11 | 0.97 | 0.78 | 1.4 |
| SRM100 _{M7} | -5.36 | -4.9 | -4.09 | 7.82 | 7.32 | 7.13 | 2.46 | 2.42 | 3.04 |

Table S1. Absorbed radiation (cross section of fitted line and y-axes in FigS12 and FigS13) in SAI simulations.